Antibody Self-Assembly Maximizes Cytoplasmic Immunostaining Accuracy of Compact Quantum Dots

Liang Ma,[††] Junlong Geng,[††] Vladimir L. Kolossov, Zhiyuan Han, Yi Pei, Sung Jun Lim, Kristopher A. Kilian, and Andrew M. Smith*

ACCESS | Metrics & More | Article Recommendations | Supporting Information

ABSTRACT: Antibody conjugates of quantum dots (QDs) are expected to transform immunofluorescence staining by expanding multiplexed analysis and improving target quantification. Recently, a new generation of small QDs coated with multidentate polymers has improved QD labeling density in diverse biospecimens, but new challenges prevent their routine use. In particular, these QDs exhibit nonspecific binding to fixed cell nuclei and their antibody conjugates have random attachment orientations. This report describes four high-efficiency chemical approaches to conjugate antibodies to compact QDs. Methods include click chemistry and self-assembly through polyhistidine coordination, both with and without adaptor proteins that directionally orient antibodies. Specific and nonspecific labeling are independently analyzed after application of diverse blocking agent classes, and a new assay is developed to quantitatively measure intracellular labeling density based on microtubule stain connectivity. Results show that protein conjugation to the QD surface is required to simultaneously eliminate nonspecific binding and maintain antigen specificity. Of the four conjugation schemes, polyhistidine-based coordination of adaptor proteins with antibody self-assembly yields the highest intracellular staining density and the simplest conjugation procedure. Therefore, antibody and adaptor protein orientation, in addition to blocking optimization, are important determinants of labeling outcomes, insights that can inform translational development of these more compact nanomaterials.
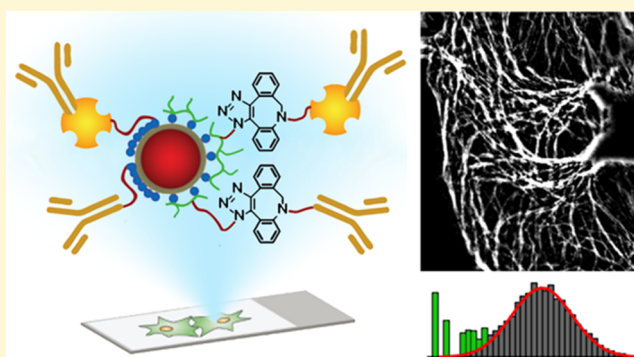
INTRODUCTION

Immunofluorescence staining is widely used in the biomedical sciences to determine the locations of proteins within cells and tissues.[1,2] In most common methods, contrast derives from fluorescent dyes covalently attached to an antibody (Ab) that selectively binds, either directly or indirectly, to a specific target protein. Many advantages have been reported when dyes are replaced with light-emitting semiconductor nanocrystals called quantum dots (QDs).[3,4] QDs provide a broader range of emission colors due to their multispectral tunability by size and composition[5] and allow bright emission in the infrared where tissue autofluorescence is diminished relative to the visible spectrum.[6] QDs also enhance detection sensitivity due to improved brightness, increase stain longevity due to higher photochemical stability compared with dyes,[3,4] and provide correlative contrast by electron microscopy due to high electron density.[7] But despite these advantages, QDs have not been widely adopted in immunostaining workflows, largely due to ongoing challenges related to their colloidal nature. Problems include conjugate instability and inaccurate staining patterns due to steric hindrance deriving from their large sizes, which are too large to diffuse and distribute throughout fixed cells and tissues that are densely packed with macro-

molecules.[6,8−10] The detrimental impact of size is well documented for diverse classes of staining agents,[11−15] and hence there is an ongoing effort to shrink the size of current QDs from ca. 25−35 nm to <10 nm, below the size of an Ab.[16]

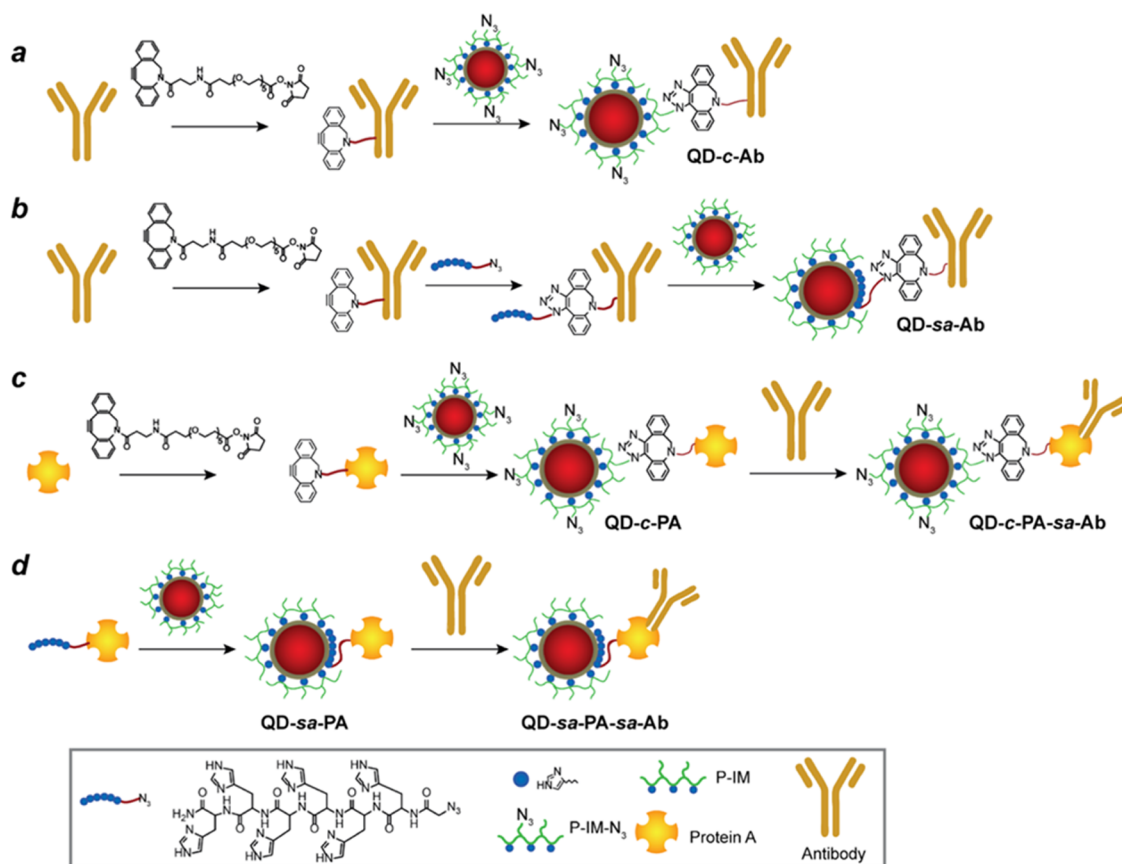Multidentate polymeric ligands are now widely applied as coatings to prepare smaller QDs.[17−25] These polymers are multifunctional, combining metal-coordinating functional groups that adhere to the QD surface, hydrophilic groups that instill aqueous colloidal stability and prevent nonspecific binding, and reactive domains for efficient chemical attachment to Abs. QDs coated with multidentate polymers have been particularly beneficial for dynamic imaging of membrane receptors on living cells,[26−29] but new challenges prevent use in fixed cells. Specifically, questions remain regarding how to eliminate nonspecific binding of these smaller materials to intracellular microenvironments rich in basic chemical groups

Scheme 1. Schematic Illustration of the Syntheses of Four Quantum Dot Antibody (QD-Ab) Conjugates through High-Efficiency Click Chemistry and Self-Assembly, with or without Protein A (PA) Adaptor Proteins[a]

[a](a) QD-*c*-Ab: Ab modified with dibenzylcyclooctyne-(ethylene glycol)$_5$-*N*-hydroxysuccinimide (DBCO-EG$_5$-NHS) ester conjugates to azide-functional QDs through click chemistry. (b) QD-*sa*-Ab: Ab modified with DBCO-EG$_5$-NHS ester conjugates to azide-His-tag to obtain His-tag Ab, which self-assembles with QDs. (c) QD-*c*-PA-*sa*-Ab: PA modified with DBCO-EG$_5$-NHS ester conjugates to azide-QDs through click chemistry to generate QD-*c*-PA, which self-assembles with Ab Fc domains. (d) QD-*sa*-PA-*sa*-Ab: His-tag-PA self-assembles with QDs through His-tag linkers to generate QD-*sa*-PA, which self-assembles with Ab Fc domains.

(*vide infra*) and how to optimally attach these QDs to Abs. Compact QDs are similar in size and charge to commonly used IgG Abs, so purification of reaction products using methods based on physicochemical properties may not be feasible. Standard amide-generating reactions based on *N*-hydroxysuccinimide (NHS) esters and thioether-generating reactions between maleimides and thiols are widely used for larger QDs,[30] but for smaller QDs, unreacted Abs in the products cannot be readily removed. Newer click chemistries, such as strain-promoted alkyne-azide cycloaddition (SPAAC) and inverse-electron-demand Diels−Alder cycloaddition are advantageous for these applications due to their higher efficiency in aqueous solution, yielding nearly complete reactions and eliminating the need for purification of the conjugates.[31−33] Moreover, these reactions are more controllable, resulting in predictable product valency and minimal cross-linking-induced aggregation that is common for polyfunctional macromolecule coupling using activated esters.

Chemical conjugation methods for Abs often result in random orientation between an Ab and its label.[34] Therefore, for a nanoparticle-Ab conjugate, some of the antigen-binding Fab domains of the Ab cannot sterically access antigen targets. For this reason, molecular adaptors such as Protein A, Protein G, and Fc receptor fragments are useful, as they bind to the Fc domain of the Ab, which is distal from the Fab domains.[35,36] In

this scenario, the adaptor proteins are first attached to the QD to allow attachment to an Ab with Fab oriented outward from the surface, without the necessity to chemically modify the Ab.[25,36] Protein A (PA) is especially useful because it can bind to Fc domains from numerous Ab species, yielding a nearly universe platform for fast preparation of QD-Ab libraries through self-assembly.[37]

A unique protein conjugation mechanism for QDs is self-assembly with metal-binding functional groups. This is most widely applied using oligo-histidine (His) peptide tags (His-tags),[38] which coordinate metal ions such as zinc and nickel in aqueous solution. When recombinantly expressed on protein termini, His-tags bind rapidly and quantitatively to QDs with a dissociation equilibrium constant near 1 nM, resulting in conjugates with near-zero linker length.[24,39−42] This reaction chemistry also allows oriented attachment of the protein to the surface, so functional domains are directed away from the QD surface. This process works for QDs coated with monolayers of small ligands or multidentate polymer coatings, although the means by which this occurs on QDs with densely packed polymer coatings remains to be determined. This His-tag-based conjugation modality appears to be incompatible with QDs coated with thicker amphiphilic polymer-based bilayers, which are mainstays of commercial QD products.[41]
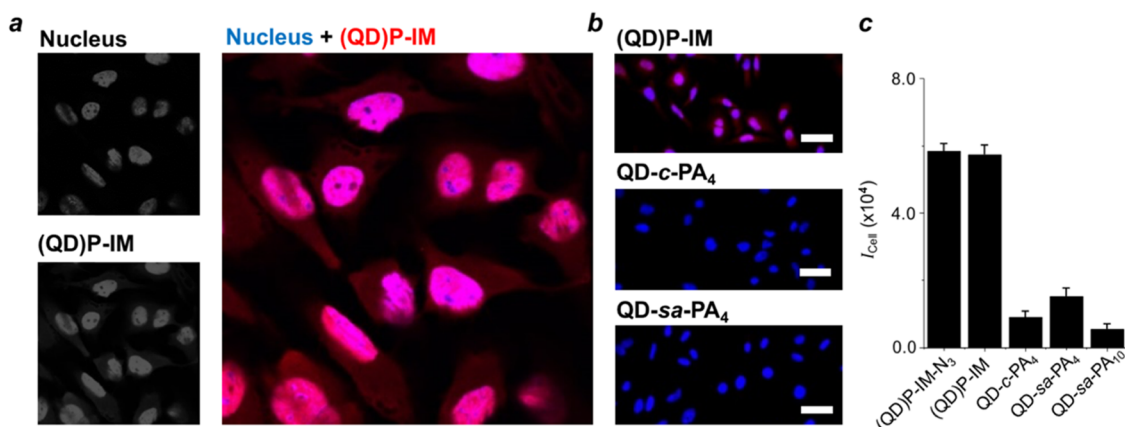
Figure 1. Nonspecific nuclear binding of compact QDs and reduction by protein conjugation. (a) Fluorescence confocal micrographs of fixed and permeabilized HeLa cells treated with QDs coated with P-IM, showing separate Hoechst nuclear stain channel and QD channel. The two-color overlay of nucleus (blue) and QD (red) channels shows diffuse nuclear labeling. (b) Two-color overlay of nuclear (blue) and QD (red) channels are shown for HeLa cells treated with QDs coated with P-IM as well as QD-*c*-PA$_4$ and QD-*sa*-PA$_4$. (c) Fluorescence intensity per cell (I_{cell}) for cells treated with indicated QD samples. Mean values are shown with error bars indicating standard deviation.

Here, we report four high-efficiency conjugation schemes to attach Abs to compact QDs coated with multifunctional multidentate ligands together with an analysis of the independent impacts of adaptor proteins and oriented attachment. Scheme 1 shows that QDs are attached to Abs through combinations of covalent click chemistry (*c*) and self-assembly (*sa*). Directly conjugated QD-Ab conjugates are indicated as QD-*c*-Ab for covalent click chemistry or QD-*sa*-Ab for self-assembly, with the latter using Abs modified to contain His-tags. Two indirect QD-Ab conjugates are generated using QDs bound to the adaptor protein PA through covalent click chemistry (QD-*c*-PA-*sa*-Ab) or His-tag self-assembly (QD-*sa*-PA-*sa*-Ab). We previously reported syntheses of QD-*c*-Ab and QD-*sa*-PA conjugates using compact QDs,[25] but direct performance comparisons across diverse classes of QD-Ab conjugates for staining applications have not been reported. We use near-infrared (NIR) QDs with 720 nm emission to enable sensitive detection of target molecules in autofluorescent cells and tissues and focus on primary labeling of tubulin targets, which are densely distributed throughout the cytoplasm of cells. The distinctive patterns of microtubule labels are useful for the assessment of labeling accuracy through high-resolution fluorescence microscopy, which allowed us to design a cytoplasmic staining assay that can be widely applied to evaluate label performance in crowded environments. We find that nonspecific binding is enhanced in the nuclei for these small QDs but can be eliminated using electrostatic blocking agents or protein adsorption to the QD surface. Pairwise comparisons show that random attachment orientation of Abs has the most detrimental impact on labeling performance, and QD-*sa*-PA-*sa*-Ab conjugates prepared entirely through self-assembly performed the best for intracellular microtubule labeling. Further development of self-assembly with Abs for QDs stands to have a major impact on scaled-up production and diverse immunofluorescence applications of these materials.

■ RESULTS AND DISCUSSION

Synthesis and Characterization of Compact, Near-Infrared QDs. QDs composed of (core)shell $(Hg_xCd_{1-x}Se_yS_{1-y})Cd_zZn_{1-z}S$ were synthesized through mercury cation exchange of ternary $CdSe_yS_{1-y}$ alloy cores to red-

shift the fluorescence emission to the NIR, followed by epitaxial growth of 4.7 monolayers of $Cd_zZn_{1-z}S$ to boost the quantum yield (QY) and stability (see the Experimental Section).[43] The QDs had an average core diameter of 4.5 nm from transmission electron microscopy (Figure S1), with a bright fluorescence emission peak at 720 nm (Figure S2). The QDs were phase-transferred to water after coating with multidentate polymeric ligands containing imidazole binding groups and oligoethyleneglycol (OEG) hydrophilic groups terminated entirely with hydroxyls (P-IM) or partially terminated with azides (P-IM-N$_3$) for covalent SPAAC click reactions. The resulting aqueous QDs were monodisperse in size based on size exclusion chromatography (SEC), with a mean hydrodynamic diameter of 11 nm derived from globular protein size standards (Figure S3), a size similar to IgG Abs. These results indicate that the polymers are compactly attached on the surface. After purification, the QY in aqueous solution was approximately 30% based on fluorescein as a standard. These QDs are stable in phosphate-buffered saline (PBS, pH 7.4) at 4 °C, with monodispersity retained after about 2 years by SEC (Figure S4).

Compact QDs Nonspecifically Label Cell Nuclei. Previously, we observed that compact QDs coated with P-IM or P-IM-N$_3$ exhibit little nonspecific binding to fixed, permeabilized cells due to the presence of a high graft density of electrostatically neutral OEG compared with QDs coated with anionic polymeric ligands.[25] However, further examination of these unconjugated QDs under conditions needed for high-resolution imaging of low-copy-number antigens and single-molecule imaging reveals that QDs are adsorbed diffusely throughout the nuclei of fixed, permeabilized cells (Figure 1a). To determine the cause and eliminate this effect, we evaluated the impact of initially treating cells with a diverse range of blocking agents before QD application. Colloidal agents like serum albumin, casein, and nonfat milk exhibited negligible impact, whereas metal ions such as Zn^{2+} or Ni^{2+}, or anionic polymers such as dextran sulfate or polyacrylic acid substantially reduced nuclear labeling (Figure S5a). These results suggest that nonspecific binding of nonfunctional compact QDs is similar to that of a basophilic dye stain,[44] which can be neutralized by polyacids and metals. The mechanism is that many nuclear proteins like histones are rich
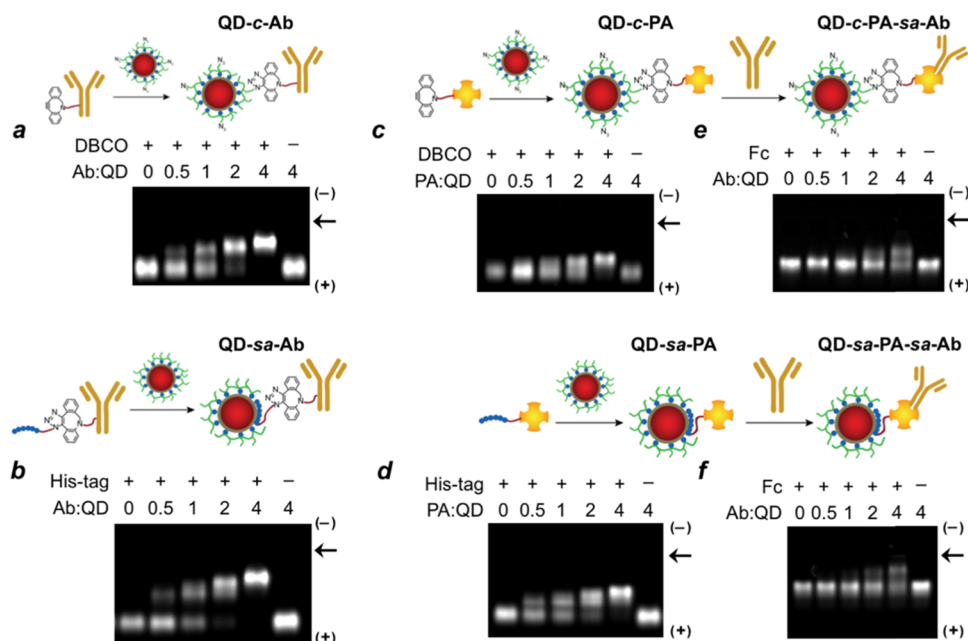
Figure 2. Characterization of QD-PA and QD-Ab conjugation products by gel electrophoresis. (a) QD-*c*-Ab conjugation using indicated molar ratios between DBCO-Ab and (QD)P-IM-N$_3$, including a control for Ab not modified with DBCO. (b) QD-*sa*-Ab conjugation using indicated molar ratios between His-tag-Ab and (QD)P-IM, including a control for Ab not modified with His-tags. (c) QD-*c*-PA conjugation using indicated molar ratios between DBCO-PA and (QD)P-IM-N$_3$, including a control using PA not modified with DBCO. (d) QD-*sa*-PA conjugation using indicated molar ratios between His-tag-PA and (QD)P-IM, including a control using PA without His-tag. (e) QD-*c*-PA-*sa*-Ab conjugation using indicated molar ratios between QD-*c*-PA and Ab, including a control using Ab with Fc domain removed. (f) QD-*sa*-PA-*sa*-Ab conjugation using indicated molar ratios between QD-*sa*-PA and Ab, including a control using Ab with Fc domain removed. Reactions in (a−d) were conducted for 12 h at room temperature. Reactions in (e) and (f) were conducted for 2 h at room temperature.

in metal-coordinating moieties such as arginines, lysines, and histidines that can bind to QD surface facets through the same mechanism as His-tags and the imidazole-based P-IM polymer, resulting in nuclear accumulation. Divalent cations and polyanions adsorb these native groups to make them inaccessible for QDs to bind. This effect likely arises from the displacement of the polymeric ligand by these proteins, which bind directly to the QD surface, as inferred from studies described below involving proteins bearing His-tags.

Nuclear Labeling Can Be Eliminated by Adsorbed Proteins. While pre-blocking treatment with metals or polyanions eliminated nonspecific binding of compact QDs, it also eliminated specific labeling of QD-Ab conjugates (Figure S5b), reflecting a chemical perturbation that also disrupts target antigens. To avoid antigen-depleting treatments, we observed that protein conjugates of compact QDs exhibited significantly less nonspecific binding to cell nuclei. As shown in Figure 1b,c, compared with QDs only coated with P-IM, the fluorescence intensity of HeLa cells reduced by a factor of 3 for QD-*c*-PA$_4$, for which QDs were conjugated to PA through a covalent linkage at a ratio of 4:1 PA:QD. Significant reduction of nonspecific binding was also observed for QD-*sa*-PA$_4$ for which PA is attached through His-tag self-assembly. For the latter QD, there was a further reduction in nonspecific binding by increasing the PA:QD ratio to 10. This nonspecific binding reduction can be attributed to blocking of the QD surface by PA, which shields the basophilic QD surface from basic nuclear proteins. Therefore, a design rule for compact QD-Ab conjugates to avoid nonspecific binding is to eliminate free, unconjugated QDs in the conjugate population.

Synthesis and Characterization of QD-Antibody Conjugates. Four classes of QD conjugates were designed

and synthesized using anti-α-tubulin IgG2b (αtAb) as a model Ab to take advantage of distinctive cytoplasmic staining patterns to assess target binding specificity. Isotype control IgG2b Abs (icAb) were used throughout to quantify labeling deriving from nonspecific effects. PA was used as a recombinantly expressed adaptor protein with or without (native) a terminal His-tag. Both native PA and Abs were covalently modified to contain dibenzylcyclooctyne (DBCO) through NHS coupling to protein amines using the reagent DBCO-(ethylene glycol)$_5$-NHS (DBCO-EG$_5$-NHS). DBCO incorporation measured by ultraviolet absorption spectrophotometry (Figure S6) was determined to be 6.6, 4.1, and 6.2 DBCO per protein for αtAb, icAb, and PA, respectively. These products react with azide-bearing QDs or peptides (Scheme 1a−c). To generate Abs that self-assemble with QDs through His-tags, we generated a clickable azide-functional His-tag adaptor by solid-phase peptide synthesis as shown in Scheme 1b, with structure confirmed by mass spectrometry and >90% purity confirmed by HPLC (Figure S7). After mixing in excess with DBCO-functionalized Abs and purification, complete reaction of the DBCO groups with azido peptides was evident from the disappearance of the DBCO absorption band at 309 nm (Figure S8), resulting in ∼6 His-tags per Ab. Importantly, DBCO incorporation occurs on diverse lysine and N-terminal groups in proteins, which could disrupt protein function and reduce antigen binding affinity. However, compared with the unmodified αtAb, no significant change in intensity was observed for these modified Abs based on indirect immunofluorescence staining (Figure S9), suggesting negligible impact on antigen-binding sites.

Figure 2 shows gel electrophoresis characterization of QD-Ab conjugates prepared as shown in Scheme 1, with reactant

stoichiometries tuned to evaluate reaction efficiencies, product valencies, and reaction specificity. These QDs are slight anionic at basic pH, resulting in migration toward the positive electrode. Conjugation to proteins with similar charge density as the QDs results in reduced electrophoretic mobility due to an increase in hydrodynamic size. QDs coated with P-IM-N$_3$ were conjugated to DBCO-Ab through covalent click chemistry to yield QD-c-Ab (Figure 2a), resulting in a progressive reduction of the free QD band with increasing DBCO-Ab ratios. There was a proportional increase in the intensity of a band with reduced mobility corresponding to Ab conjugates, while no reaction was evident when the Ab was not conjugated to DBCO, indicating specificity of the reaction. Figure 2b shows a similar trend for QD-sa-Ab, for which His-tag Abs were conjugated through self-assembly to QDs coated with P-IM. These latter conjugates also demonstrated specificity in requiring a His-tag functional group. It is noteworthy that Xia and co-workers showed that multivalent His-tags can increase association rates for self-assembly up to 50-fold compared with single His-tag counterparts,[45−47] so Abs bearing ~6 His-tags could have unique benefits for the rapid preparation of stable conjugates.

Figure 2c,d shows electrophoretic characterizations of reactions using PA adaptor proteins bound to the QD through covalent conjugation or self-assembly. Gel electrophoresis results show similar trends to those for direct Ab conjugations, but with a smaller degree of band-shift between the free QDs and conjugates as a result of the lower molecular weight of PA (42 kDa) compared with Ab (155 kDa). We used QD-PA conjugates at a 4:1 PA:QD ratio to proceed with self-assembly with Abs, chosen due to near-complete reaction with QDs (see below) to eliminate nonspecific nuclear labeling (Figure 1b,c). Figure 2e,f shows results for reaction mixtures between different amounts of Ab with either QD-c-PA$_4$ or QD-sa-PA$_4$, showing a progressive development of a new band with reduced migration relative to the QD-PA conjugates. This new band is absent when using Fab$_2$ Ab fragments missing the Fc domain where PA binds.

High reaction efficiencies are evident in both the covalent and self-assembly-based attachment mechanisms. Mattoussi and co-workers previously showed that QD-protein conjugate distributions follow Poisson statistics for protein:QD ratios well below the saturation limit of the QD surface area available for Hist-tag binding.[48] Using gel electrophoresis, individual components of the QD-PA and QD-Ab conjugate populations cannot be discretely resolved; however, the free QD band is well resolved. We evaluated the relative intensities of free QDs from the four conjugation reactions and found that they were consistent with a Poisson association process with high reaction efficiencies (≥90%, Figure S10). As a result, the QD-labeled proteins should exceed any unlabeled proteins by at least 10-fold in concentration in the resulting product mixture. One notable exception is for QD-c-PA, as small differences in migration distances made gel analysis imprecise so we have less certainty of its product stoichiometries and purity, although its performance in staining applications was one of the best (see below). For 4:1 protein:QD reactions, the products are expected to have 2% or fewer free QDs, with the most prevalent components of the population bearing 3−4 proteins per QD (Figure S11). We note that addition of more proteins would be expected to further increase the mean valency of protein-QD conjugates in the product population and further deplete free QDs that are prone to nuclear

adsorption. However, this would further increase the average hydrodynamic size and further broaden the conjugate population distribution.

Figure 3 shows SEC chromatograms of conjugation reaction products. We used a slightly larger QD for these reactions so
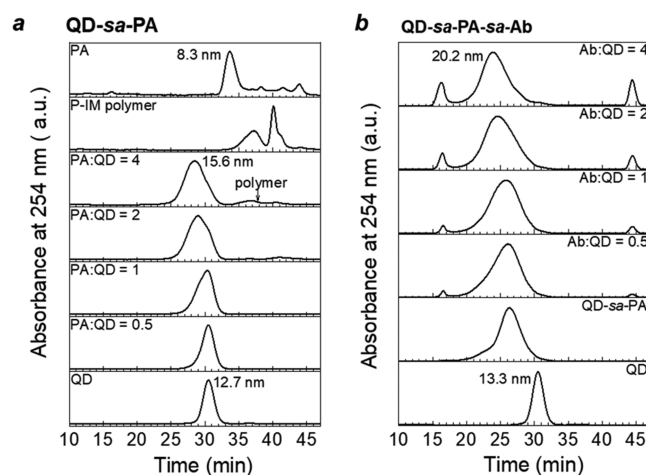

Figure 3. Characterization of QD-sa-PA and QD-sa-PA-sa-Ab conjugation reactions by size exclusion chromatography. (a) Chromatograms show QDs, PA, and their QD-sa-PA conjugates, in addition to free coating polymer (P-IM). (b) Chromatograms show QDs, QD-sa-PA conjugates, and QD-sa-PA-sa-Ab conjugates. Peaks between 40 and 45 min correspond to small molecules and salts that elute with the solvent. Peaks at 16 min correspond to the column void volume.

that their elution time did not overlap significantly with the Ab elution time. With PA self-assembly, the size incrementally increases with PA:QD ratio, leading to disappearance of the QD peak at a PA:QD ratio of 4, with no evidence of free PA remaining in the reaction mixture (Figure 3a). However, a low-molecular-weight peak appears with increasing PA:QD corresponding in retention time to the free P-IM polymer that coats the QDs. This suggests that the His-tag on PA displaces the polymer, which is in line with its presumed mechanism of conjugation to the QD by direct coordination to the surface metal atoms. The final median size of QD-sa-PA$_4$ (15.6 nm) corresponds by volume to the size of a QD plus four PA proteins, together with the release of 11 polymers. The size of the QD-sa-PA conjugate also grows incrementally with the addition of Ab (Figure 3b), reaching a median diameter of 20.2 nm at Ab:QD = 4. This matches the expected size of this QD-PA complex with the addition of four proteins, each is 10 nm in diameter, which is near the size of the Ab measured by SEC. Covalent QD-c-Ab conjugates with the same conjugation ratio were smaller (Figure S12), and both classes of QD-Ab conjugates were smaller than commonly used commercial variants with a similar emission wavelength (Qdot-705-IgG; 23.4 nm; Figure S13). We further note that QDs and other colloids can be adsorbed by globular proteins in biological media and in blocking solutions to further increase the total size of the conjugates. In this work, we use 1% solutions of bovine serum albumin in all performance studies, conditions that we previously found yield a protein corona on bare QDs.[49] Based on fluorescence correlation spectroscopy measurements (Figure S14), the P-IM-coated QDs used in this work exhibited a ~3 nm increase in radial hydrodynamic thickness in BSA solutions (p = 0.0033, Table S1). However, the QD
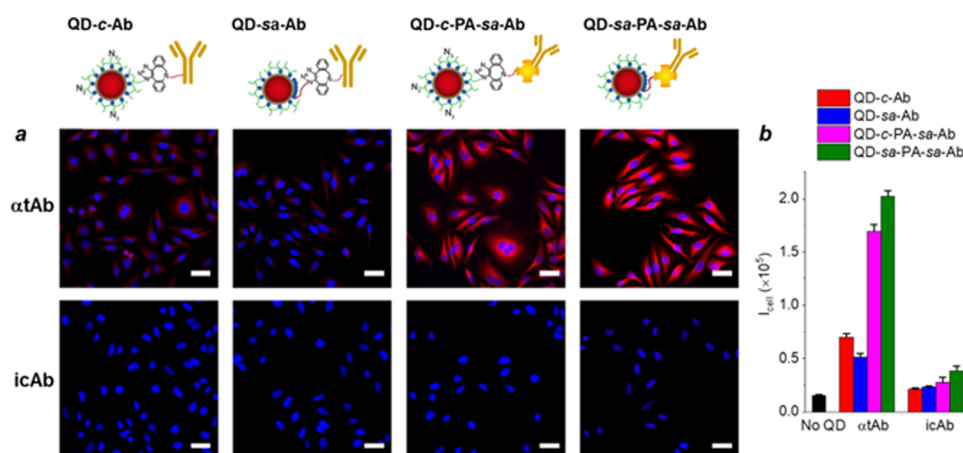
Figure 4. Direct immunofluorescence staining with four classes of QD-Ab probes. (a) Representative 20× fluorescence micrographs of HeLa cells show labeling with probes using αtAb (top row) or icAb (bottom row). Blue color is nuclear Hoechst stain, and red color is the QD channel. Scale bar: 50 μm. (b) Fluorescence intensity per cell (I_{cell}) for cells treated with indicated QD-Ab samples. Mean values are shown with error bars indicating standard deviation. Statistical comparisons by Student's t-test are provided in Table S2.

conjugates of PA and Ab were unaltered in size in the presence of BSA ($p > 0.20$) indicating that the proteins shield the probe from corona formation, which is consistent with their lack of nonspecific nuclear labeling (Figure 1).

Immunolabeling Specificity and Intensity. We next compared the immunostaining performance of QD-Ab₄ conjugates prepared using the four reaction mechanisms in Scheme 1. QD-PA₄ was used for conjugates that included adaptor proteins. Each of the four conjugates were applied at an equal concentration of QDs and Abs but intrinsic differences in conjugate distributions, Ab orientation, and potential Ab functionality may impact staining performance. We used a single-step direct immunolabeling protocol in which the QD-Ab conjugates of αtAb or icAb were added to fixed and permeabilized HeLa cells. Figure 4a shows representative fluorescence micrographs, showing red fluorescence in the cytoplasmic region for αtAb conjugates, with little fluorescence measured in nuclei, consistent with the elimination of nuclear labeling (Figure 1). Nonspecific labeling with icAb conjugates was much lower than specific labeling for all four conjugate classes.

Quantitative fluorescence intensity per cell is shown in Figure 4b. Different conjugation methods led to different outcomes in both specific and nonspecific staining. Self-assembly of the unmodified Ab using PA adaptor proteins yielded substantially higher specific staining compared to QD conjugates in which Abs were covalently modified and attached to QDs directly. In particular, the signal intensity of QD-sa-PA-sa-Ab was 5.2 times higher than that of QD-sa-Ab ($p < 0.001$) and 3.4 times higher than that of QD-c-Ab ($p < 0.001$), suggesting that Ab orientation plays an important role in staining density. QD-sa-Ab exhibited the lowest staining intensity overall and was significantly worse than QD-c-Ab ($p < 0.001$), which was also conjugated directly. The covalently modified Abs used for these two conjugates were equivalent when applied as secondary stains (Figure S9) and are expected to exhibit similar Ab orientations upon conjugation, as they were derived from the same NHS-DBCO derivatives. The lower staining intensity for QD-sa-Ab may therefore be due to conformational modifications of the His-tag Ab driven by self-assembly to the rigid QD surface compared with covalent conjugation to the flexible polymer coating for QD-c-Ab.

Conjugation through covalent attachment to the QD polymer may therefore preserve the Ab conformation more than when it adsorbs to the QD surface.

Paradoxically, attachment of the Ab through PA also increased nonspecific binding of icAb conjugates. In fact, QD-sa-PA-sa-Ab showed the highest specific labeling intensity and the highest nonspecific binding, so the signal-to-background ratio (7.8) was significantly lower than that of the QD-c-PA-sa-Ab conjugate (12.9; $p < 0.001$). The higher background binding for indirect PA-based conjugates compared with direct Ab conjugates likely arose from the smaller size of PA (42 kDa) compared with Abs (155 kDa). As background binding appears to derive from direct interactions between QD surfaces and nuclear proteins, a larger protein directly bound to the QD surface may more effectively shield the QD surface. This is also consistent with higher background labeling observed for His-tag conjugations (QD-sa-Ab and QD-sa-PA-sa-Ab) compared with covalent conjugations (QD-c-Ab and QD-c-PA-sa-Ab) ($p < 0.05$), as proteins extend further from the surface when attached through click chemistry to the polymer coating. This is further consistent with the additional reduction in nonspecific binding for QD-sa-PA₁₀ compared with QD-sa-PA₄ (Figure 2). The inferior performance of QD-Ab conjugates generated through covalent conjugation is also consistent with previous reports. For example, Pathak et al. demonstrated that commercial conjugation kits using thiol-maleimide reactions yielded fewer than 0.1 functional Ab per QD.[50] Tasso et al. also determined that QD-Ab conjugates generated by thiol-maleimide reactions using larger QDs had 3-fold fewer functional Abs compared with those made through self-assembly with PA.[29]

We validated that fully self-assembled QD-sa-PA-sa-Ab conjugates can be used to stain fresh frozen breast tumor tissue and formalin-fixed, paraffin-embedded (FFPE) brain tissues (Figure S15). An absence of nuclear staining was observed for 5−6 μm sections for both tissue classes using QD-αtAb conjugates while untreated controls showed similar intensities as QD-icAb conjugates. These results suggest that self-assembled QD-sa-PA-sa-Ab is suitable for staining more complex, heterogeneous biospecimens with high autofluorescence. QDs can be particularly beneficial for such applications due to their strong emission in the NIR spectrum
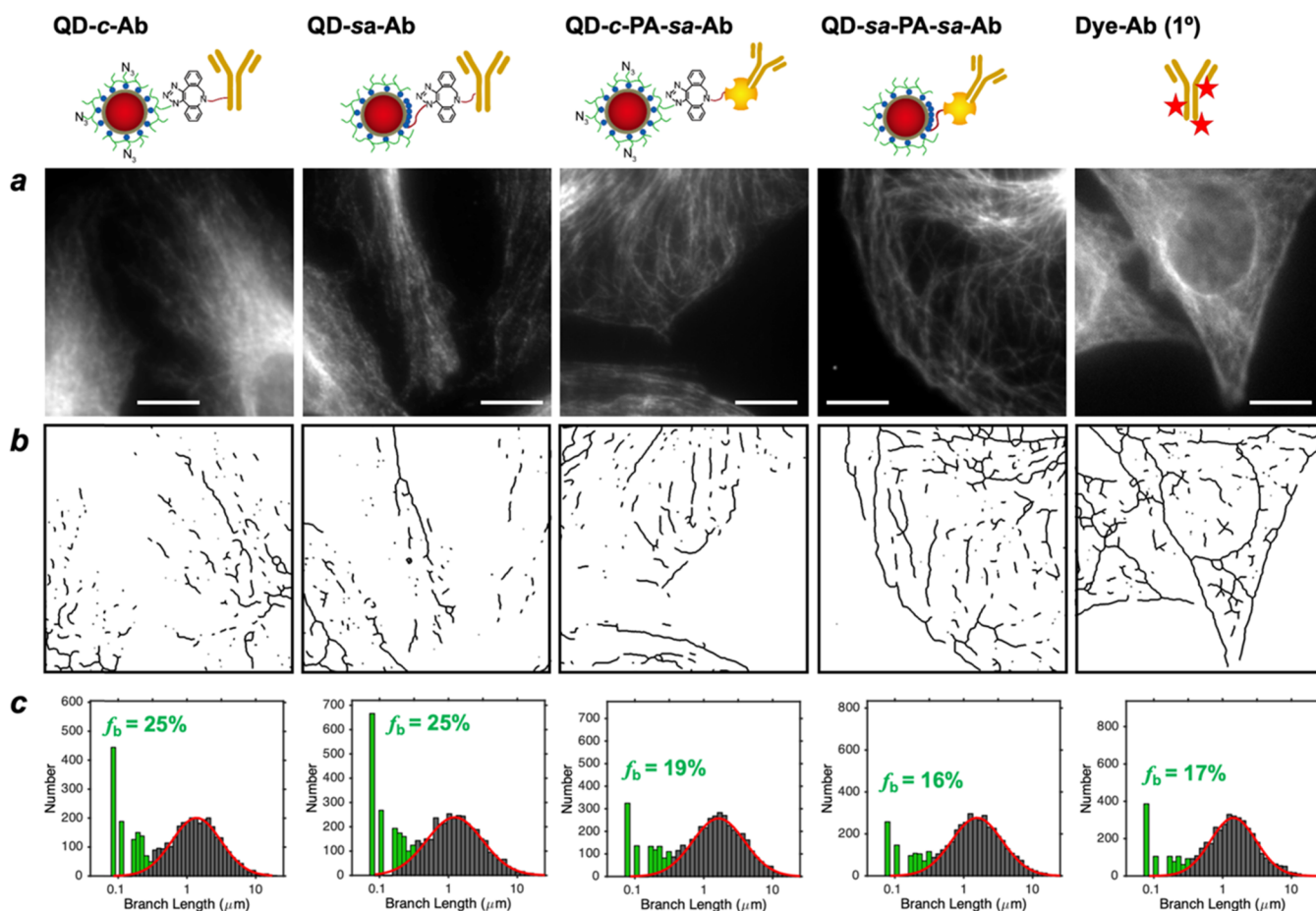
Figure 5. Microtubule connectivity measurements of HeLa cells from stains using the four QD-Ab conjugates and a Dye-Ab validation control. (a) Representative 100× TIRF micrographs of fixed and permeabilized HeLa cells stained by the indicated QD-Ab conjugates using identical conditions and concentrations of QDs and Abs. Scale bar: 5 μm. (b) Skeletonized maps of the images from (a). (c) Histogram of branch lengths for microtubules with log-normal fit in red. The fraction of branches that are broken (f_b) is given for each histogram and indicated by the highlighted green bars.

in which autofluorescence is lower in intensity compared with visible wavelengths normally used for imaging.[51] Typical dyes exhibit much weaker emission in the NIR compared with QDs.

Microtubule Connectivity Analysis Shows Benefit of Ab Self-Assembly. To further evaluate the staining performance of these QD-Ab conjugates for labeling diffraction-limited structures, microtubule connectivity was measured through morphological image analysis.[53] Microtubules are cytoskeletal proteins composed of tubulin protein polymers distributed throughout the cytoplasm with micron-scale lengths and 24 nm widths.[54] Mapping the connectivity of microtubule networks at super-resolution is playing an important role in understanding fundamental cellular processes, such as motility, intracellular transport, and polarization during development.[55] Challenges for mapping at high resolution in 3D derive from label photobleaching,[54] which could be potentially overcome using QDs, which are highly photostable. However, because QDs are larger than traditional stains, steric hindrance may leave unlabeled gaps in the network. Figure 5 shows representative high-resolution fluorescence micrographs of QD stains of microtubules in HeLa cells (Figure 5a), together with connectivity maps derived from skeletonized images (Figure 5b). Microtubule length histograms are shown for 4000 to 6000 branches for each QD class (Figure 5c) and for dye-based primary immunostain using the same Ab. For

densely stained samples, branch lengths were characterized by log-normal distributions centered near 1.5 μm. There was a significant difference between the four conjugates in the fraction of branches that were disconnected, reflected by short-length peaks, with many contributed by diffraction-limited spots. This under-connectivity derives from insufficient staining density of the microtubules.

The staining density for the four conjugates followed the same trends as total staining intensity (Figure 4), as QD-sa-PA-sa-Ab provided the best connectivity preservation with fewer isolated spots, with even better performance than primary dye-Ab stains. Only 16% of the branches were disconnected compared with 25% for QD-c-Ab and QD-sa-Ab, which exhibited the lowest connectivity network with the highest number of isolated spots. This outcome likely derives from the low functionality of the Ab on the two direct QD-Ab conjugates. The staining performance of QD-sa-PA-sa-Ab was also superior to that of QD-c-PA-sa-Ab (19% disconnected branches), a structure that has been used in several previous QD imaging studies.[37,53,56] This difference may be due to the more random orientation of Abs on QD-c-PA-sa-Ab due to the randomness of covalent attachment of PA to the QD surface. We also performed a control study in which dye-labeled PA was allowed to self-assemble with Ab in solution prior to labeling cells. Images of the labeled cells showed large fractions

of broken tracks (26%, Figure S16), likely due to the ability of PA to cross-link multiple Ab and potentially generate large products. It is noteworthy that the performance of the QD-*sa*-PA-*sa*-Ab conjugate surpassed that of the primary dye immunostain (Figure 5) and matched that of a secondary immunostain (16% broken tracks, Figure S15). In total, QD-*sa*-PA-*sa*-Ab matched the performance metrics of the best dye-based labels that are the standard of the field at present. These single-color QD-*sa*-PA-*sa*-Ab probes have immediate advantages compared with dye-based reagents due to their simplicity of production through mixing without purification, whereas dyes require purification after conjugation to antibodies. The probes can be used rapidly after conjugation, but we also found that similar self-assembled conjugates are stable for at least 24 h at room temperature at a concentration of 100 nM or higher (above the dissociation constant of the His-tag interaction with the QD surface).[52] Further advantages of these QD-Ab probes will derive from their capacity for quantitative single-molecule imaging, long-term photostability, and high-dimensional multiplexing.

CONCLUSIONS

The broad application of immunofluorescence methods throughout the life sciences has recently accelerated due to developments in single-molecule[57−60] and super-resolution fluorescence imaging.[61−66] QDs stand to make a major impact in these fields due to their wide multispectral tunability, stability, and improved single-molecule quantification accuracy, providing bright signals from direct immunostains without the need for secondary labeling. However, after nearly 20 years of testing, they are still only used in niche applications, such as studies of live-cell receptor dynamics.[67] Toward a new generation of QD reagents that are ultrastable, off-the-shelf, and adaptable to diverse uses, QDs with small sizes stand to make a major impact by overcoming previous problems of low staining specificity in addition to labeling patterns that do not match those of standardized stains. QD-*sa*-PA-*sa*-Ab may meet these demands by providing high staining intensity for cytoplasmic targets with a simple conjugation workflow, simply requiring sequential mixing of three reagents that spontaneously self-assemble, without the need for purification. These probes should be directly compatible with modern workflows for labeling and label stripping that increase multiplexing capacity by orders of magnitude.[37,68] While strong performance is evident for cultured cells and thin tissue sections, it remains to be determined whether or not these probes are adequately compact for applications requiring perfusion through three-dimensional tissues, such as optically cleared intact tissues or cultured spheroids and organoids. It should be noted that other recombinant molecular adaptors like Protein G, Protein A/G, and Fc receptor fragments can be applied in the same manner to prepare QD-Ab conjugates,[36,69] and these same conjugation methods may also be applied to broader categories of nanoparticles with unique optical properties.[70,71] Future work will focus on determining the degree to which staining depends on antigen classes and identifying components within conjugate populations that are primarily responsible for high-density staining.

EXPERIMENTAL SECTION

Materials. Polyimidazole ligands (P-IM and P-IM-N$_3$) and cadmium behenate were prepared in our previous work.[25] Milli-Q purified water was used throughout. Unless specified, all other chemicals and solvents were purchased from Sigma-Aldrich and used without further purification.

QD Synthesis. (Core)shell (Hg$_x$Cd$_{1−x}$Se$_y$S$_{1−y}$)Cd$_z$Zn$_{1−z}$S nanocrystals with emission at 720 nm were synthesized and purified according to published protocols[43] with a few modifications. First, CdSe$_y$S$_{1−y}$ alloy cores (d = 2.8 nm; λ_{abs} = 506 nm) were synthesized by heating a vacuum-dried mixture (~100 °C, 1 h) of cadmium behenate (0.2 mmol), selenium dioxide (0.13 mmol), sulfur powder (0.07 mmol), and 1,2-hexadecanediol (0.2 mmol) in 1-octadecene (4 mL) to 230 °C under nitrogen, allowing 15 min reaction at this temperature. The resulting cores were then purified and dispersed chloroform (~100 nmol in 5 mL) at room temperature before addition of a mercury acetate solution in oleylamine (0.2 M) with a 2-fold excess of mercury relative to the total amount of cadmium. After ~5 min, cation exchange was quenched by injection of 1-octanethiol (~100 μL) and the QDs were precipitated with a methanol/acetone mixture (1:1 v/v; ~20 mL). The QDs were further purified by three cycles of dispersion in hexane (~10 mL) with oleylamine (~100 μL) and oleic acid (~100 μL), followed by precipitation with methanol/acetone (~20 mL). The resulting Hg$_x$Cd$_{1−x}$Se$_y$S$_{1−y}$ QDs with a first exciton absorption peak at 640 nm were stored as a stock solution in hexane. Cd$_z$Zn$_{1−z}$S shells were grown epitaxially on the cores through standard layer-by-layer shell growth with 0.8-monolayer (ML) increments, generating 2.4 ML CdS, 0.8 ML Cd$_{0.75}$Zn$_{0.25}$S, and 1.5 ML ZnS. Cadmium acetate in oleylamine (0.1 M), zinc acetate in oleylamine (0.1 M), and elemental sulfur in 1-octadecene were used as Cd, Zn, and S precursors, respectively. The resulting QDs had a first exciton absorption peak at 680 nm and a single emission peak at 720 nm. The QDs were purified by precipitation from acetone, dispersed in hexane, and stored at −20 °C until use.

Polymer Coating of QDs. Purified QDs in hexane were phase-transferred to *N*-methylformamide (NMF) by dropwise addition of tetramethylammonium hydroxide (TMAH, 25 wt % in methanol) at 100 equivalents to QD surface atoms. P-IM or P-IM-N$_3$ dissolved in dimethyl sulfoxide (DMSO) (11.3 mg/mL, 150 μL) was mixed with the hydroxide-coated QDs in NMF (8.41 μM, 237.8 μL) at a 5:1 ratio of imidazoles to QD surface atoms. The solution was purged with nitrogen for 2 min and then stirred at 110 °C for 2 h before precipitation with a mixture of ether and chloroform. The QDs were collected by centrifugation, dried, and dispersed in 50 mM sodium borate buffer (pH 8.5). Excess polymer was removed by centrifugal filtration (Amicon Ultra 50 kDa MWCO) with dilution and filtration repeated four times.

Synthesis of Azido-hexahistidine. The azido-hexahistidine peptide was synthesized by standard Fmoc solid-phase synthesis as described previously.[72] In a typical reaction, 20% piperidine in dimethylformamide (DMF) was mixed with N-terminal fluorenylmethyloxycarbonyl (Fmoc)-protected Rink amide resin for 15 min to remove Fmoc protecting groups. After filtration, the resin was collected and rinsed with DMF four times. A DMF mixture of amino acid (3 equiv), *N*-methylmorpholine and benzotriazol-1-yl-oxy-tripyrrolidinophosphonium hexafluorophosphate (PyBOP) was added and incubated with the resin for 2 h at room temperature under vigorous stirring. The reaction was halted by filtration to collect the resin, followed by four washes with DMF. Coupling and deprotection was assessed by a standard ninhydrin test. At the final step, the peptides were capped with 2-azidoacetic acid in DMF overnight. Then, the resin was incubated with a mixture containing 95% trifluoroacetic acid (TFA), 2.5% H$_2$O, and 2.5% triisopropylsilane for 3 h. The peptides were cleaved from the resin and the resin was removed by filtration. The peptides were further purified by precipitation in ice-cold diethyl ether and three dissolution/precipitation cycles using TFA/ether. Finally, the peptides were dissolved in water and dried by lyophilization. The purity of azido-hexahistidine was determined by semipreparative reversed-phase high-performance liquid chromatography (RP-HPLC, PerkinElmer Flexar). ESI-MS (low resolution, positive mode): calculated for C$_{38}$H$_{46}$N$_{22}$O$_7$, *m/z* 462.5 [M + 2H]$^+$/2; found 462.5 [M + 2H]$^+$/2.

DBCO-Ab Synthesis. Mouse monoclonal IgG2b αtAb (Proteintech catalog no. 66031-1-Ig) and icAb (Invitrogen catalog no. 02-

65300) were purified to remove sodium azide before the addition of a solution of DBCO-EG$_5$-NHS (2.5 mM in anhydrous DMSO, Click Chemistry Tools) at 10 times the molar equivalent of Ab. The mixture was incubated at room temperature for 30 min before the reaction was quenched with the addition of Tris-HCl (1 M, pH 8.5, 5 μL). The mixture was incubated for 5 min at room temperature before purification by centrifugal filtration (Amicon Ultra MWCO 50 kDa) against PBS five times. Absorption spectra of the Ab solutions were acquired to determine the number of DBCO per Ab using the absorption at 280 and 309 nm according to the product manual from Click Chemistry Tools.

DBCO-PA Synthesis. Native PA (Fisher-Pierce catalog no. 21181) in PBS was mixed with a solution of DBCO-EG$_5$-NHS (5 mM in anhydrous DMSO) at 10 times the molar equivalent of PA. The mixture was incubated at room temperature for 30 min before the reaction was quenched by addition of Tris-HCl (1 M, pH 8.5, 5 μL). The mixture was incubated for 5 min at room temperature before purification by centrifugal filtration (Amicon Ultra MWCO 3 kDa) against PBS five times. The concentration of PA was measured using a bicinchoninic acid protein assay (Pierce catalog no. 23225). The number of DBCO incorporated in the PA conjugate was determined by ultraviolet spectrophotometry as described above.

His-tag-Ab Synthesis. Freshly prepared DBCO-Ab was mixed with azido-hexahistidine at a 10:1 peptide:Ab molar ratio at room temperature overnight with gentle shaking. After reaction, unreacted peptide was removed by centrifugal filtration (Amicon Ultra MWCO 50 kDa) against PBS four times. Conjugation was verified by the disappearance of the characteristic DBCO absorption peak at 309 nm using a NanoDrop spectrophotometer.

QD-*c*-PA and QD-*c*-Ab Synthesis. P-IM-N$_3$-coated QDs in sodium phosphate buffer (10 mM, pH 7.4) were mixed at different ratios with freshly prepared DBCO-Ab or DBCO-PA at room temperature overnight. Then, a 50-fold molar excess of 2-azidoacetic acid was added to the solution to quench remaining DBCO, followed by 15 min of reaction at room temperature. Conjugates were characterized by polyacrylamide-agarose gel electrophoresis.

QD-*sa*-PA and QD-*sa*-Ab Synthesis. P-IM-coated QDs in sodium phosphate buffer (10 mM, pH 7.4) were mixed with different ratios of His-tag-Ab or His-tag-PA at room temperature for 4 h. Conjugates were characterized by polyacrylamide-agarose gel electrophoresis.

QD-*c*-PA-*sa*-Ab and QD-*sa*-PA-*sa*-Ab Synthesis. QD-*c*-PA and QD-*sa*-PA were mixed with Ab at room temperature for 4 h. Conjugates were characterized by polyacrylamide-agarose gel electrophoresis.

Cell Culture. HeLa cells (ATCC #CCL2) were cultured in Eagles' minimum essential medium (EMEM) with 10% fetal bovine serum (FBS) and 1% penicillin/streptomycin (P/S) at 37 °C in 5% CO$_2$.

Evaluation of Nonspecific Binding to HeLa Cells. HeLa cells were seeded at a density of 5×10^4 cells per well on 12 mm circular coverglass in 24-well plates and cultured for 24 h. The cells were washed three times with PBS before fixation with freshly prepared 4% paraformaldehyde (PFA) for 20 min at room temperature. The cells were washed (PBS 3×), permeabilized (0.1% Triton X-100 in PBS for 20 min), and washed again (PBS 3×). The cells were then blocked for 1 h with 1 wt % bovine serum albumin (BSA), except in the case of specifically noted blocking conditions. The cells were then washed (PBS 3×) and 40 nM dispersions of QDs were added, using either QDs coated with P-IM, QDs coated with P-IM-N$_3$, QD-*sa*-PA, or QD-*c*-PA, each in 1 wt % BSA solution. The cells were incubated for 1 h at room temperature. Control experiments were carried out by incubating cells without QDs. The cells were washed (PBS 3×), and nuclei were stained with Hoechst 33258 (2 μg/mL). Coverglass was then mounted with 90% glycerol in PBS on a glass slide, sealed with nail polish. For epifluorescence imaging, the cells were imaged immediately on a Zeiss Axio Observer Z1 inverted microscope with an EC Plan-Neofluar 20× 0.50 NA air objective. Hoechst was excited with 100 W halogen lamp illumination with a 365 nm excitation filter, and emitted light was passed through a 445/50 nm bandpass filter; QDs were excited with 100 W halogen lamp illumination with a 488

nm excitation filter, and emitted light was passed through a 732/68 nm bandpass filter. Images were obtained using a Photometrics eXcelon Evolve 512 EMCCD camera controlled by Zeiss ZEN software. Images from all control and QD samples were collected using identical imaging conditions. For confocal imaging, the cells were imaged with a Leica SP8 UV/visible laser confocal microscope using a 63× 1.4 N.A. oil objective.

Antibody Validation by Secondary Labeling. HeLa cells were seeded at a density of 5×10^4 cells per well in a Lab-Tek glass-bottom eight-well chamber and cultured for 20 h. The cells were then fixed with 4% PFA for 20 min, permeabilized with 0.1% (v/v) Triton X-100 for 20 min, and blocked with 1% BSA for 1 h. The cells were then incubated with αtAb, DBCO-αtAb, or His-tag-αtAb in 1% BSA overnight at 4 °C. After washing, the cells were incubated with a secondary Ab conjugated to Alexa 647 at room temperature and then stained with Hoechst (2 μg/mL) for 10 min. The cells were imaged using the same instrument and conditions as described above for QDs but with a 594 nm excitation filter and 732/68 nm bandpass emission filter. Images from all control and dye samples were collected using identical imaging conditions.

Immunofluorescence Staining of HeLa Cells with QD-Ab and Dye-Ab Conjugates. HeLa cells were seeded at a density of 5×10^4 cells per well in a Lab-Tek glass-bottom eight-well chamber and cultured for 20 h. The cells were then fixed with 4% PFA for 20 min, permeabilized with 0.1% (v/v) Triton X-100 for 20 min, and blocked with 1% BSA for 1 h. For QD-based labels, the cells were incubated with 25 nM QD-Ab conjugates in 1% BSA at room temperature for 2 h and stained with Hoechst (2 μg/mL) for 10 min. Three staining protocols were used for dye-based labels. For primary immunolabeling, an Alexa 488-labeled αtAb (25 nM) in 1% BSA was incubated with cells at room temperature for 2 h. For secondary immunolabeling, the cells were first incubated with unlabeled αtAb (25 nM) before incubation with Alexa 488-labeled secondary antibody (50 nM) at room temperature for 2 h. For dye-PA labeling, Alexa 488-labeled PA (25 nM) was mixed with unlabeled αtAb in 1% BSA and incubated with cells at room temperature for 2 h. To collect 20× images, the cells were imaged using the same instrument and conditions as described above for QDs. For 100× images, QDs and dyes were imaged in total internal reflectance fluorescence (TIRF) mode with 488 nm laser excitation with 100× 1.45 NA α Plan-Fluar oil immersion objective. Images from all treatments were collected using identical imaging conditions.

Microtubule Branch Length Quantification. Fluorescent microtubule stains imaged at 100× in HeLa cells were exported as 8-bit TIFFs before denoising using a custom MATLAB script, treating all images identically. The images were then imported into ImageJ, processed with a Gaussian blur, and thresholded to generate a mask that was processed with the Skeletonize (2D/3D) and Analyze Skeleton (2D/3D) scripts to extract microtubule maps and branch lengths. The long-branch half of the length histogram was fit to a log-normal distribution, and the area of overlap was used to calculate the percent of branches outside the distribution. At least 11 images were used for each QD class, yielding 4000 to 6000 branches.

Immunofluorescence Staining of Fresh Tumor Tissue with QD-Ab Conjugates. Mouse breast tumors were fixed with 4% PFA for 24 h and embedded in optimum cutting temperature (O.C.T.) compound before sectioning using a cryostat at a thickness of 6 μm. The samples were air-dried on slides and stored at −80 °C. Tissue sections were permeabilized (0.1% Triton X-100 in PBS) for 20 min, washed (PBS 3×), and blocked (2 wt % BSA solution) for 30 min before addition of QD-Ab conjugates (40 nM) for 2 h at room temperature. The samples were then washed (PBS 3×) and stained with Hoechst (5 μg/mL) for 5 min. The slides were mounted with 90% glycerol and sealed with nail polish. The tissues were imaged using the same instrument and conditions as described above for QDs to collect 20× images, except using 488 nm laser excitation. Images from all control and QD samples were collected using identical imaging conditions.

Immunofluorescence Staining of FFPE Tumor Tissue with QD-Ab Conjugates. Paraffin-embedded formalin-fixed brain tissues

on slides were deparaffinized in xylene for 5 min and rehydrated with an ethanol gradient (from 100 to 75%). Antigens were retrieved by heating the tissue slides in a microwave oven in citrate buffer (10 mM, pH 6.1). After cooling to room temperature, the slides were washed (0.2% Triton X-100 in PBS) for 25 min and blocked with BSA solution (2 wt %) for 30 min. The slides were then incubated with QD-Ab in BSA (1 wt %) for 2 h at room temperature, washed (PBS 3×), and stained with Hoechst (5 μg/mL) for 5 min. The slides were mounted with 90% glycerol and sealed with nail polish. The tissue was imaged using the same instrument and conditions as described above. Images from all control and QD samples were collected using identical imaging conditions.

Fluorescence Correlation Spectroscopy. Protocols are described in detail in our previous reports.[49,52] Briefly, QDs and their conjugates were diluted to 10 nM in PBS or PBS containing 1% BSA. Time-series fluorescence at 0.1 MHz was recorded for 10 s in eight-well glass-bottom Lab-Tek chambers with excitation by a diode laser (470 nm). Rhodamine B (diffusion coefficient = 4.2×10^{-10} m^2 s^{-1}) was used as a standard to calibrate the confocal spot size. Diffusion coefficients were calculated from the Brownian motion model, and hydrodynamic diameters were calculated using the Stokes−Einstein equation.[49]

Instrumentation. Fluorescence spectra were measured using a NanoLog Horiba Jobin Yvon (HORIBA Scientific) with data collected using Fluo Essence V3.5 software. Ultraviolet−visible absorption spectra were obtained using a Cary series UV−VIS−NIR spectrophotometer (Agilent Technologies) with data collected using Cary WinUV Scan Application Version 6.00 1551 software. For fluorescence QY measurements, the solution was diluted to absorption of ∼0.1 at 490 nm. QY was calculated relative to a reference dye (fluorescein in 10 mM NaOH, QY = 92%). FCS data were collected with an Alba FCS instrument (ISS) with single-photon avalanche photodiode detector. Gel electrophoresis of QDs was conducted using our published protocol.[25] Transmission electron microscopy (TEM) images were obtained using a JEOL 2010 LaB6 high-resolution microscope in the Frederick Seitz Materials Research Laboratory Central Research Facilities at University of Illinois. Size exclusion chromatography for QDs was performed on an ÄKTApurifier UPC10 (GE Healthcare) with a Superose Increase 6 10/300GL column (GE Healthcare Bio-Sciences AB) with data processed with UNICORN 5.31 Workstation software.

■ ASSOCIATED CONTENT

Ⓢ Supporting Information

The Supporting Information is available free of charge at https://pubs.acs.org/doi/10.1021/acs.chemmater.1c00164.

Electron micrographs of QDs, optical spectra of QDs, size exclusion chromatograms of QDs, fluorescence micrographs of cells for blocking solution optimization, DBCO functionalization data, azido-hexahistidine chromatogram, Ab absorption spectra, fluorescence micrographs of cells stained with dye-Ab conjugates, QD-protein conjugate distribution analysis, distribution models, size exclusion chromatograms of QD-Ab conjugates, FCS analyses of QDs and QD-protein conjugates, fluorescence micrographs of tissues stained with QD-Ab conjugates, microtubule connectivity data from cells labeled using dyes, a table of p values for FCS data, and a table of p values for fluorescence intensity per cell (PDF)

■ AUTHOR INFORMATION

Corresponding Author

Andrew M. Smith − *Department of Materials Science and Engineering, University of Illinois at Urbana-Champaign, Urbana, Illinois 61801, United States; Holonyak Micro and Nanotechnology Laboratory, Department of Bioengineering, Carl R. Woese Institute for Genomic Biology, and Cancer Center at Illinois, University of Illinois at Urbana-Champaign, Urbana, Illinois 61801, United States; Carle Illinois College of Medicine, Urbana, Illinois 61801, United States;* ⓞ orcid.org/0000-0002-0238-4816; Email: smi@illinois.edu

Authors

Liang Ma − *Department of Materials Science and Engineering, University of Illinois at Urbana-Champaign, Urbana, Illinois 61801, United States; Holonyak Micro and Nanotechnology Laboratory, University of Illinois at Urbana-Champaign, Urbana, Illinois 61801, United States;* ⓞ orcid.org/0000-0002-6102-5821

Junlong Geng − *Department of Bioengineering, Carl R. Woese Institute for Genomic Biology, and Beckman Institute for Advanced Science and Technology, University of Illinois at Urbana-Champaign, Urbana, Illinois 61801, United States;* ⓞ orcid.org/0000-0002-9738-1924

Vladimir L. Kolossov − *Holonyak Micro and Nanotechnology Laboratory and Department of Bioengineering, University of Illinois at Urbana-Champaign, Urbana, Illinois 61801, United States*

Zhiyuan Han − *Department of Materials Science and Engineering, University of Illinois at Urbana-Champaign, Urbana, Illinois 61801, United States; Holonyak Micro and Nanotechnology Laboratory, University of Illinois at Urbana-Champaign, Urbana, Illinois 61801, United States*

Yi Pei − *Department of Materials Science and Engineering, University of Illinois at Urbana-Champaign, Urbana, Illinois 61801, United States; Holonyak Micro and Nanotechnology Laboratory, University of Illinois at Urbana-Champaign, Urbana, Illinois 61801, United States; School of Materials Science and Engineering, University of New South Wales, Sydney, NSW 2052, Australia*

Sung Jun Lim − *Holonyak Micro and Nanotechnology Laboratory and Department of Bioengineering, University of Illinois at Urbana-Champaign, Urbana, Illinois 61801, United States; Division of Nanotechnology, Dalseong-Gun 42988, Republic of Korea;* ⓞ orcid.org/0000-0002-4504-597X

Kristopher A. Kilian − *Department of Materials Science and Engineering, University of Illinois at Urbana-Champaign, Urbana, Illinois 61801, United States; Holonyak Micro and Nanotechnology Laboratory and Department of Bioengineering, University of Illinois at Urbana-Champaign, Urbana, Illinois 61801, United States; School of Materials Science and Engineering and School of Chemistry, Australian Centre for NanoMedicine, University of New South Wales, Sydney, NSW 2052, Australia*

Complete contact information is available at:
https://pubs.acs.org/10.1021/acs.chemmater.1c00164

Author Contributions

[††]L.M. and J.G. equally contributed to this work.

Notes

The authors declare no competing financial interest.

■ ACKNOWLEDGMENTS

■ REFERENCES

(1) Lichtman, J. W.; Conchello, J. A. Fluorescence Microscopy. *Nat. Methods* **2005**, *2*, 910−919.

(2) Robertson, D.; Savage, K.; Reis-Filho, J. S.; Isacke, C. M. Multiple Immunofluorescence Labelling of Formalin-Fixed Paraffin-Embedded (Ffpe) Tissue. *BMC Cell Biol.* **2008**, *9*, 13.

(3) Resch-Genger, U.; Grabolle, M.; Cavaliere-Jaricot, S.; Nitschke, R.; Nann, T. Quantum Dots Versus Organic Dyes as Fluorescent Labels. *Nat. Methods* **2008**, *5*, 763−775.

(4) Wu, X.; Liu, H.; Liu, J.; Haley, K. N.; Treadway, J. A.; Larson, J. P.; Ge, N.; Peale, F.; Bruchez, M. P. Immunofluorescent Labeling of Cancer Marker Her2 and Other Cellular Targets with Semiconductor Quantum Dots. *Nat. Biotechnol.* **2003**, *21*, 41−46.

(5) Fountaine, T. J.; Wincovitch, S. M.; Geho, D. H.; Garfield, S. H.; Pittaluga, S. Multispectral Imaging of Clinically Relevant Cellular Targets in Tonsil and Lymphoid Tissue Using Semiconductor Quantum Dots. *Mod. Pathol.* **2006**, *19*, 1181−1191.

(6) Prost, S.; Kishen, R. E.; Kluth, D. C.; Bellamy, C. O. Working with Commercially Available Quantum Dots for Immunofluorescence on Tissue Sections. *PLoS One* **2016**, *11*, No. e0163856.

(7) Giepmans, B. N. G.; Deerinck, T. J.; Smarr, B. L.; Jones, Y. Z.; Ellisman, M. H. Correlated Light and Electron Microscopic Imaging of Multiple Endogenous Proteins Using Quantum Dots. *Nat. Methods* **2005**, *2*, 743−749.

(8) Ioannou, D.; Griffin, D. K. Nanotechnology and Molecular Cytogenetics: The Future Has Not yet Arrived. *Nano Rev.* **2010**, *1*, 5117.

(9) Ioannou, D.; Tempest, H. G.; Skinner, B. M.; Thornhill, A. R.; Ellis, M.; Griffin, D. K. Quantum Dots as New-Generation Fluorochromes for Fish: An Appraisal. *Chromosome Res.* **2009**, *17*, 519−530.

(10) Liu, Y.; Le, P.; Lim, S. J.; Ma, L.; Sarkar, S.; Han, Z.; Murphy, S. J.; Kosari, F.; Vasmatzis, G.; Cheville, J. C.; et al. Enhanced mRNA Fish with Compact Quantum Dots. *Nat. Commun.* **2018**, *9*, No. 4461.

(11) Cai, E.; Ge, P.; Lee, S. H.; Jeyifous, O.; Wang, Y.; Wilson, K. M.; Lim, S. J.; Baird, M. A.; Stone, J. E.; Lee, K. Y.; et al. Stable Small Quantum Dots for Synaptic Receptor Tracking on Live Neurons. *Angew. Chem.* **2014**, *126*, 12692−12696.

(12) Lee, S. H.; Jin, C. Y.; Cai, E.; Ge, P. H.; Ishitsuka, Y.; Teng, K. W.; de Thomaz, A. A.; Nall, D.; Baday, M.; Jeyifous, O.; et al. Super-Resolution Imaging of Synaptic and Extra-Synaptic AMPA Receptors with Different-Sized Fluorescent Probes. *Elife* **2017**, *6*, No. e27744.

(13) Groc, L.; Lafourcade, M.; Heine, M.; Renner, M.; Racine, V.; Sibarita, J. B.; Lounis, B.; Choquet, D.; Cognet, L. Surface Trafficking of Neurotransmitter Receptor: Comparison between Single-Molecule/Quantum Dot Strategies. *J. Neurosci.* **2007**, *27*, 12433−12437.

(14) Takizawa, T.; Robinson, J. M. Use of 1.4-nm Immunogold Particles for Immunocytochemistry on Ultra-Thin Cryosections. *J. Histochem. Cytochem.* **1994**, *42*, 1615−1623.

(15) Helma, J.; Cardoso, M. C.; Muyldermans, S.; Leonhardt, H. Nanobodies and Recombinant Binders in Cell Biology. *J. Cell Biol.* **2015**, *209*, 633−644.

(16) Smith, A. M.; Nie, S. M. Next-Generation Quantum Dots. *Nat. Biotechnol.* **2009**, *27*, 732−733.

(17) Smith, A. M.; Nie, S. Minimizing the Hydrodynamic Size of Quantum Dots with Multifunctional Multidentate Polymer Ligands. *J. Am. Chem. Soc.* **2008**, *130*, 11278−11279.

(18) Liu, W. H.; Greytak, A. B.; Lee, J.; Wong, C. R.; Park, J.; Marshall, L. F.; Jiang, W.; Curtin, P. N.; Ting, A. Y.; Nocera, D. G.; et al. Compact Biocompatible Quantum Dots Via Raft-Mediated Synthesis of Imidazole-Based Random Copolymer Ligand. *J. Am. Chem. Soc.* **2010**, *132*, 472−483.

(19) Palui, G.; Na, H. B.; Mattoussi, H. Poly(Ethylene Glycol)-Based Multidentate Oligomers for Biocompatible Semiconductor and Gold Nanocrystals. *Langmuir* **2012**, *28*, 2761−2772.

(20) Giovanelli, E.; Muro, E.; Sitbon, G.; Hanafi, M.; Pons, T.; Dubertret, B.; Lequeux, N. Highly Enhanced Affinity of Multidentate Versus Bidentate Zwitterionic Ligands for Long-Term Quantum Dot Bioimaging. *Langmuir* **2012**, *28*, 15177−15184.

(21) Zhang, P.; Liu, S.; Gao, D.; Hu, D.; Gong, P.; Sheng, Z.; Deng, J.; Ma, Y.; Cai, L. Click-Functionalized Compact Quantum Dots Protected by Multidentate-Imidazole Ligands: Conjugation-Ready Nanotags for Living-Virus Labeling and Imaging. *J. Am. Chem. Soc.* **2012**, *134*, 8388−8391.

(22) Susumu, K.; Oh, E.; Delehanty, J. B.; Pinaud, F.; Gemmill, K. B.; Walper, S.; Breger, J.; Schroeder, M. J.; Stewart, M. H.; Jain, V.; et al. A New Family of Pyridine-Appended Multidentate Polymers as Hydrophilic Surface Ligands for Preparing Stable Biocompatible Quantum Dots. *Chem. Mater.* **2014**, *26*, 5327−5344.

(23) Xu, J. M.; Ruchala, P.; Ebenstain, Y.; Li, J. J.; Weiss, S. Stable, Compact, Bright Biofunctional Quantum Dots with Improved Peptide Coating. *J. Phy. Chem. B* **2012**, *116*, 11370−11378.

(24) Lim, S. J.; Ma, L.; Schleife, A.; Smith, A. M. Quantum Dot Surface Engineering: Toward Inert Fluorophores with Compact Size and Bright, Stable Emission. *Coord. Chem. Rev.* **2016**, *320-321*, 216−237.

(25) Ma, L.; Tu, C.; Le, P.; Chitoor, S.; Lim, S. J.; Zahid, M. U.; Teng, K. W.; Ge, P.; Selvin, P. R.; Smith, A. M. Multidentate Polymer Coatings for Compact and Homogeneous Quantum Dots with Efficient Bioconjugation. *J. Am. Chem. Soc.* **2016**, *138*, 3382−3394.

(26) Tasso, M.; Giovanelli, E.; Zala, D.; Bouccara, S.; Fragola, A.; Hanafi, M.; Lenkei, Z.; Pons, T.; Lequeux, N. Sulfobetaine-Vinylimidazole Block Copolymers: A Robust Quantum Dot Surface Chemistry Expanding Bioimaging's Horizons. *ACS Nano* **2015**, *9*, 11479−11489.

(27) Lane, L. A.; Smith, A. M.; Lian, T.; Nie, S. Compact and Blinking-Suppressed Quantum Dots for Single-Particle Tracking in Live Cells. *J. Phys. Chem. B* **2014**, *118*, 14140−14147.

(28) Wang, W.; Ji, X.; Kapur, A.; Zhang, C.; Mattoussi, H. A Multifunctional Polymer Combining the Imidazole and Zwitterion Motifs as a Biocompatible Compact Coating for Quantum Dots. *J. Am. Chem. Soc.* **2015**, *137*, 14158−14172.

(29) Tasso, M.; Singh, M.; Giovanelli, E.; Fragola, A.; Loriette, V.; Frugier-Regairaz, M.; Dautry, F.; Treussart, F.; Lenkei, Z.; Lequeux, N.; et al. Oriented Bioconjugation of Unmodified Antibodies to Quantum Dots Capped with Copolymeric Ligands as Versatile Cellular Imaging Tools. *ACS Appl. Mater. Interfaces* **2015**, *7*, 26904−26913.

(30) Xing, Y.; Chaudry, Q.; Shen, C.; Kong, K. Y.; Zhau, H. E.; Chung, L. W.; Petros, J. A.; O'Regan, R. M.; Yezhelyev, M. V.; Simons, J. W.; et al. Bioconjugated Quantum Dots for Multiplexed and Quantitative Immunohistochemistry. *Nat. Protoc.* **2007**, *2*, 1152−1165.

(31) Pelaz, B.; Jaber, S.; de Aberasturi, D. J.; Wulf, V.; Aida, T.; de la Fuente, J. M.; Feldmann, J.; Gaub, H. E.; Josephson, L.; Kagan, C. R.; et al. The State of Nanoparticle-Based Nanoscience and Biotechnology: Progress, Promises, and Challenges. *ACS Nano* **2012**, *6*, 8468−8483.

(32) Kotagiri, N.; Li, Z.; Xu, X.; Mondal, S.; Nehorai, A.; Achilefu, S. Antibody Quantum Dot Conjugates Developed Via Copper-Free Click Chemistry for Rapid Analysis of Biological Samples Using a

Microfluidic Microsphere Array System. *Bioconjugate Chem.* **2014**, *25*, 1272−1281.

(33) Pickens, C. J.; Johnson, S. N.; Pressnall, M. M.; Leon, M. A.; Berkland, C. J. Practical Considerations, Challenges, and Limitations of Bioconjugation Via Azide-Alkyne Cycloaddition. *Bioconjugate Chem.* **2018**, *29*, 686−701.

(34) Agarwal, P.; Bertozzi, C. R. Site-Specific Antibody−Drug Conjugates: The Nexus of Bioorthogonal Chemistry, Protein Engineering, and Drug Development. *Bioconjugate Chem.* **2015**, *26*, 176−192.

(35) Choe, W.; Durgannavar, T. A.; Chung, S. J. Fc-Binding Ligands of Immunoglobulin G: An Overview of High Affinity Proteins and Peptides. *Materials* **2016**, *9*, 994.

(36) Kim, C.; Galloway, J. F.; Lee, K. H.; Searson, P. C. Universal Antibody Conjugation to Nanoparticles Using the Fcγ Receptor I (FcγRI): Quantitative Profiling of Membrane Biomarkers. *Bioconjugate Chem.* **2014**, *25*, 1893−1901.

(37) Zrazhevskiy, P.; Gao, X. H. Quantum Dot Imaging Platform for Single-Cell Molecular Profiling. *Nat. Commun.* **2013**, *4*, No. 1619.

(38) Clapp, A. R.; Medintz, I. L.; Mauro, J. M.; Fisher, B. R.; Bawendi, M. G.; Mattoussi, H. Fluorescence Resonance Energy Transfer between Quantum Dot Donors and Dye-Labeled Protein Acceptors. *J. Am. Chem. Soc.* **2004**, *126*, 301−310.

(39) Blanco-Canosa, J. B.; Wu, M.; Susumu, K.; Petryayeva, E.; Jennings, T. L.; Dawson, P. E.; Algar, W. R.; Medintz, I. L. Recent Progress in the Bioconjugation of Quantum Dots. *Coord. Chem. Rev.* **2014**, *263−264*, 101−137.

(40) Sapsford, K. E.; Pons, T.; Medintz, I. L.; Higashiya, S.; Brunel, F. M.; Dawson, P. E.; Mattoussi, H. Kinetics of Metal-Affinity Driven Self-Assembly between Proteins or Peptides and CdSe-Zns Quantum Dots. *J. Phys. Chem. C* **2007**, *111*, 11528−11538.

(41) Duan, H.; Kuang, M.; Wang, Y. A. Quantum Dots with Multivalent and Compact Polymer Coatings for Efficient Fluorescence Resonance Energy Transfer and Self-Assembled Biotagging. *Chem. Mater.* **2010**, *22*, 4372−4378.

(42) Liu, W.; Howarth, M.; Greytak, A. B.; Zheng, Y.; Nocera, D. G.; Ting, A. Y.; Bawendi, M. G. Compact Biocompatible Quantum Dots Functionalized for Cellular Imaging. *J. Am. Chem. Soc.* **2008**, *130*, 1274−1284.

(43) Lim, S. J.; Zahid, M. U.; Le, P.; Ma, L.; Entenberg, D.; Harney, A. S.; Condeelis, J. S.; Smith, A. M. Brightness-Equalized Quantum Dots. *Nat. Commun.* **2015**, *6*, No. 8210.

(44) Kiernan, J. A. Does Progressive Nuclear Staining with Hemalum (Alum Hematoxylin) Involve DNA, and What Is the Nature of the Dye-Chromatin Complex? *Biotech. Histochem.* **2018**, *93*, 133−148.

(45) Wang, J.; Xia, J. Preferential Binding of a Novel Polyhistidine Peptide Dendrimer Ligand on Quantum Dots Probed by Capillary Electrophoresis. *Anal. Chem.* **2011**, *83*, 6323−6329.

(46) Wang, J.; Jiang, P.; Han, Z.; Qiu, L.; Wang, C.; Zheng, B.; Xia, J. Fast Self-Assembly Kinetics of Quantum Dots and a Dendrimeric Peptide Ligand. *Langmuir* **2012**, *28*, 7962−7966.

(47) Lu, Y.; Wang, J.; Wang, J.; Wang, L.; Au, S. W.-N.; Xia, J. Genetically Encodable Design of Ligand "Bundling" on the Surface of Nanoparticles. *Langmuir* **2012**, *28*, 13788−13792.

(48) Pons, T.; Medintz, I. L.; Wang, X.; English, D. S.; Mattoussi, H. Solution-Phase Single Quantum Dot Fluorescence Resonance Energy Transfer. *J. Am. Chem. Soc.* **2006**, *128*, 15324−15331.

(49) Le, P.; Vaidya, R.; Smith, L. D.; Han, Z.; Zahid, M. U.; Winter, J.; Sarkar, S.; Chung, H. J.; Perez-Pinera, P.; Selvin, P. R.; et al. Optimizing Quantum Dot Probe Size for Single-Receptor Imaging. *ACS Nano* **2020**, *14*, 8343−8358.

(50) Pathak, S.; Davidson, M. C.; Silva, G. A. Characterization of the Functional Binding Properties of Antibody Conjugated Quantum Dots. *Nano Lett.* **2007**, *7*, 1839−1845.

(51) Le, P.; Lim, S. J.; Baculis, B. C.; Chung, H. J.; Kilian, K. A.; Smith, A. M. Counting Growth Factors in Single Cells with Infrared Quantum Dots to Measure Discrete Stimulation Distributions. *Nat. Commun.* **2019**, *10*, No. 909.

(52) Han, Z.; Sarkar, S.; Smith, A. M. Zwitterion and Oligo-(Ethylene Glycol) Synergy Minimizes Nonspecific Binding of Compact Quantum Dots. *ACS Nano* **2020**, *14*, 3227−3241.

(53) Yang, X.; Zhanghao, K.; Wang, H.; Liu, Y.; Wang, F.; Zhang, X.; Shi, K.; Gao, J.; Jin, D.; Xi, P. Versatile Application of Fluorescent Quantum Dot Labels in Super-Resolution Fluorescence Microscopy. *ACS Photonics* **2016**, *3*, 1611−1618.

(54) Kandel, M. E.; Teng, K. W.; Selvin, P. R.; Popescu, G. Label-Free Imaging of Single Microtubule Dynamics Using Spatial Light Interference Microscopy. *ACS Nano* **2017**, *11*, 647−655.

(55) Li, J.; Shariff, A.; Wiking, M.; Lundberg, E.; Rohde, G. K.; Murphy, R. F. Estimating Microtubule Distributions from 2D Immunofluorescence Microscopy Images Reveals Differences among Human Cultured Cell Lines. *PLoS One* **2012**, *7*, No. e50292.

(56) Zrazhevskiy, P.; True, L. D.; Gao, X. Multicolor Multicycle Molecular Profiling with Quantum Dots for Single-Cell Analysis. *Nat. Protoc.* **2013**, *8*, 1852−1869.

(57) Thompson, M. A.; Casolari, J. M.; Badieirostami, M.; Brown, P. O.; Moerner, W. Three-Dimensional Tracking of Single Mrna Particles in Saccharomyces Cerevisiae Using a Double-Helix Point Spread Function. *Proc. Natl. Acad. Sci. U.S.A.* **2010**, *107*, 17864−17871.

(58) Li, G.-W.; Xie, X. S. Central Dogma at the Single-Molecule Level in Living Cells. *Nature* **2011**, *475*, 308−315.

(59) Kusumi, A.; Tsunoyama, T. A.; Hirosawa, K. M.; Kasai, R. S.; Fujiwara, T. K. Tracking Single Molecules at Work in Living Cells. *Nat. Chem. Biol.* **2014**, *10*, 524−532.

(60) Wu, B.; Buxbaum, A. R.; Katz, Z. B.; Yoon, Y. J.; Singer, R. H. Quantifying Protein-mRNA Interactions in Single Live Cells. *Cell* **2015**, *162*, 211−220.

(61) Yildiz, A.; Forkey, J. N.; McKinney, S. A.; Ha, T.; Goldman, Y. E.; Selvin, P. R. Myosin V Walks Hand-over-Hand: Single Fluorophore Imaging with 1.5-nm Localization. *Science* **2003**, *300*, 2061−2065.

(62) Dickson, R. M.; Cubitt, A. B.; Tsien, R. Y.; Moerner, W. E. On/Off Blinking and Switching Behaviour of Single Molecules of Green Fluorescent Protein. *Nature* **1997**, *388*, 355−358.

(63) Betzig, E.; Patterson, G. H.; Sougrat, R.; Lindwasser, O. W.; Olenych, S.; Bonifacino, J. S.; Davidson, M. W.; Lippincott-Schwartz, J.; Hess, H. F. Imaging Intracellular Fluorescent Proteins at Nanometer Resolution. *Science* **2006**, *313*, 1642−1645.

(64) Rust, M. J.; Bates, M.; Zhuang, X. W. Sub-Diffraction-Limit Imaging by Stochastic Optical Reconstruction Microscopy (STORM). *Nat. Methods* **2006**, *3*, 793−795.

(65) Huang, B.; Jones, S. A.; Brandenburg, B.; Zhuang, X. W. Whole-Cell 3D Storm Reveals Interactions between Cellular Structures with Nanometer-Scale Resolution. *Nat. Methods* **2008**, *5*, 1047−1052.

(66) Thompson, M. A.; Lew, M. D.; Moerner, W. E. Extending Microscopic Resolution with Single-Molecule Imaging and Active Control. *Annu. Rev. Biophys.* **2012**, *41*, 321−342.

(67) Kairdolf, B. A.; Smith, A. M.; Stokes, T. H.; Wang, M. D.; Young, A. N.; Nie, S. M. Semiconductor Quantum Dots for Bioimaging and Biodiagnostic Applications. *Annu. Rev. Anal. Chem.* **2013**, *6*, 143−162.

(68) Chen, K. H.; Boettiger, A. N.; Moffitt, J. R.; Wang, S.; Zhuang, X. Spatially Resolved, Highly Multiplexed RNA Profiling in Single Cells. *Science* **2015**, *348*, aaa6090.

(69) Xu, H.; Xu, J.; Wang, X.; Wu, D.; Chen, Z. G.; Wang, A. Y. Quantum Dot-Based, Quantitative, and Multiplexed Assay for Tissue Staining. *ACS Appl. Mater. Interfaces* **2013**, *5*, 2901−2907.

(70) Li, J.; Pu, K. Development of Organic Semiconducting Materials for Deep-Tissue Optical Imaging, Phototherapy and Photoactivation. *Chem. Soc. Rev.* **2019**, *48*, 38−71.

(71) Miao, Q.; Xie, C.; Zhen, X.; Lyu, Y.; Duan, H.; Liu, X.; Jokerst, J. V.; Pu, K. Molecular Afterglow Imaging with Bright, Biodegradable Polymer Nanoparticles. *Nat. Biotechnol.* **2017**, *35*, 1102−1110.

(72) Zhang, D.; Kilian, K. A. Peptide Microarrays for the Discovery of Bioactive Surfaces That Guide Cellular Processes: A Single Step

Azide−Alkyne "Click" Chemistry Approach. *J. Mater. Chem. B* **2014**, 2, 4280−4288.